



TECHNICAL ARTICLE

Nickel Superalloy Turbine Blade Parts Printed by Laser Powder Bed Fusion: Thermo-Mechanical Post-processing for Enhanced Surface Integrity and Precipitation Strengthening

D.A. Lesyk, S. Martinez, O.O. Pedash, B.N. Mordyuk, V.V. Dzhemelinskyi, and A. Lamikiz

Submitted: 15 September 2021 / Revised: 26 January 2022 / Accepted: 7 February 2022 / Published online: 28 February 2022

The combined thermo-mechanical technique for the post-processing of heat-resistant alloy parts fabricated by a 3D laser powder bed fusion (L-PBF) process is applied. In this study, the turbine blade test parts were printed using a nickel-based pre-alloyed INCONEL (IN) 718 powder. The hot isostatic pressing (HIP) followed by homogenization and double aging post-printing heat treatments was conducted to form a homogeneous structure of the L-PBF-built turbine blade parts, reducing the material porosity. The shot peening (SP) technique was applied to eliminate surface defects and provide a new surface texture, refining the grains in the subsurface layer. The effects of the post-heat treatments combined with mechanical surface SP treatment on the microstructure, phase/chemical composition, grain refinement, subsurface porosity, and microhardness distribution in the near-surface layers were studied in this work. The surface defects and roughness are also addressed. Results indicate that the HIP treatment followed by both used heat treatments provides the required uniformity of microstructure and distribution of the second phase precipitates in the L-PBF-built turbine blade parts, providing an increase in hardness by ~50%. Additionally, the application of the SP treatment after heat treatments led to a further surface hardening and increases the residual stress values. At the same time, the surface defects were successfully removed from the heat-treated surfaces by severe plastic deformation.

Keywords aging, HIP, homogenization, Inconel 718 powder, laser powder bed fusion, shot peening

1. Introduction

The oxidation- and corrosion-resistant superalloys are widely applied for manufacturing the responsible parts, which work in extreme environments subjected to high mechanical loads. It is well-known that nickel-based alloys are difficult metals to machine or shape using conventional manufacturing

techniques (casting, forging, and powder metallurgy) because of rapid strain hardening. Nowadays, additive manufacturing (AM) or three-dimensional (3D) printing techniques contribute to the expansion of the manufacturing facility, including Inconel (IN) superalloys (Ref 1-3). The current results show that the superalloy complexly shaped parts fabricated by 3D powder bed fusion technologies contain a good strength and high-temperature performance, making superalloys an attractive choice for high-temperature applications. As a result, the 3D-built superalloys are promising for the aerospace, automotive, and nuclear industries (Ref 4).

Currently, the powder bed fusion (PBF) (Ref 1, 2, 5-7), direct energy deposition (DED) (Ref 6, 7), binder jetting (BJ), or material jetting (MJ) (Ref 8, 9) techniques are proposed to

This invited article is part of a special issue in the *Journal of Materials Engineering and Performance* entitled “Space and Aerospace Exploration Revolution: Metal Additive Manufacturing.” The issue was organized by Shahrooz Nafisi, Relativity Space; Paul Gradl, NASA Marshall Space Flight Center; Douglas Hofmann, NASA Jet Propulsion Laboratory/California Institute of Technology; and Reza Ghomashchi, The University of Adelaide, Australia.

D.A. Lesyk, Laser Systems and Advanced Technologies Department, National Technical University of Ukraine “Igor Sikorsky Kyiv Polytechnic Institute”, 37 Peremohy ave., 03056 Kyiv, Ukraine; Physical Principles for Surface Engineering Department, G.V. Kurdyumov Institute for Metal Physics of the NAS of Ukraine, 36 Academician Vernadskyi blvd., 03142 Kyiv, Ukraine; and Mechanical Engineering and Mechatronics Department, West Pomeranian University of Technology, 17 Aleja Piastow, 71899 Szczecin,

Poland; **S. Martinez**, Aeronautics Advanced Manufacturing Center, University of the Basque Country, 202 Bizkaia Science and Technology Park, 48170 Zamudio, Spain; **O.O. Pedash**, MOTOR SICH JSC, 15 Motorobudivnykiv ave., 69068 Zaporizhzhia, Ukraine; **B.N. Mordyuk**, Physical Principles for Surface Engineering Department, G.V. Kurdyumov Institute for Metal Physics of the NAS of Ukraine, 36 Academician Vernadskyi blvd., 03142 Kyiv, Ukraine; **V.V. Dzhemelinskyi**, Laser Systems and Advanced Technologies Department, National Technical University of Ukraine “Igor Sikorsky Kyiv Polytechnic Institute”, 37 Peremohy ave., 03056 Kyiv, Ukraine; and **A. Lamikiz**, Aeronautics Advanced Manufacturing Center, University of the Basque Country, 202 Bizkaia Science and Technology Park, 48170 Zamudio, Spain; and Mechanical Engineering Department, University of the Basque Country, Alameda de Urquijo s/n, 48013 Bilbao, Spain. Contact e-mails: lesyk_d@ukr.net mordyuk@imp.kiev.ua.

manufacture the 3D metal components that are difficult or impossible to obtain using traditional production processes. It should be noted that to fabricate the small-sized and complexly shaped metal parts with a high density, the PBF method, including the laser powder bed fusion (L-PBF) and electron beam melting (EBM) processes, is one of the most effective 3D printing technologies, in which selectively melts metal powder by a movable laser or electron beam (Ref 10-12). The density of the PBF-manufactured IN 718 alloy is about 99.8%. However, at the same time, the PBF-built superalloy parts suffer from an inhomogeneous structure (Ref 13-15), significant residual subsurface porosity (Ref 16), rough surface (Ref 17), surface defects (Ref 18), and the presence of tensile residual stresses in the near-surface layers (Ref 19). At the same time, the structure and surface roughness values depend on build orientation.

To use the 3D-printed nickel-based alloys in extreme environments, the post-processing issue is one of the main challenges. As a consequence, the thermal and chemical or mechanical post-treatments are mostly required to improve the superalloy parts printed by the PBF techniques. The implementation of hot isostatic pressing (HIP) and post-heat treatment (stress-relieving, solution, homogenization, and aging) in the additive manufacturing routes could minimize or eliminate bulk defects in the PBF-built superalloys (Ref 20-23). In particular, the stress-relieving (SR) treatment (650-870 °C) is used before removing a part from the build plate to reduce residual stress (Ref 20). The HIP treatment (1120-1240 °C, 100-165 MPa, 3-4 h) is usually applied to eliminate porosity and increase the density for high-temperature applications (Ref 20, 24-26). The HIP treatment of superalloys combined with other thermal techniques in different sequences (applied prior or post them) was recently studied as well. For instance, work by Kuo (Ref 27) shows that the HIP treatment followed by the direct aging treatment was the most effective technique among the heat treatments to improve the creep behavior of IN 718 alloy.

The solution annealing (930-1040 °C) or homogenization (1040-1200 °C) treatments followed by a double aging/precipitation treatment are applied for the improvement of material properties (Ref 20, 28, 29). The effects of the heat treatments on microstructural features of the superalloys are studied in the subsequent works (Ref 30-32). Raghavan, et al. (Ref 30) reported the solution (1040-1200 °C) + double aging (720 °C/8 h and 620 °C/8 h) treatment induced the needle-shaped δ , carbides (MC and/or $M_{23}C_6$) within the grain boundaries, and finely dispersed γ'' , γ' phases, improving the tensile strength for all heat-processed L-PBF-built IN 718 alloy specimens. Muñiz-Lerma et al. (Ref 31) confirmed that the cuboidal primary γ' precipitates and secondary γ'' precipitates were also observed in the L-PBF-printed IN 738 alloy after annealing + aging. The effects of the post-heat treatments on the microstructure and mechanical properties of the nickel-based alloys are studied by Brenne et al. (Ref 33) and by Fayed et al. (Ref 34). Moreover, work by Barros (Ref 35) showed that the compressive residual stresses were identified in the subsurface layer of the heat-processed IN 718 alloy samples.

On the other hand, to enhance surface properties in the metal parts fabricated by the PBF technique, mechanical or chemical surface post-treatments are frequently required after heat treatments. The mechanical (machining, sanding, blasting, peening, and tumbling) or chemical (pickling and descaling) surface treatments can be selected based on the operational

requirements, geometry complexity (presence of hidden surfaces/holes), size of components, and surface quality requirements. The surface finishing of the 3D-printed metal components often demands enhanced/expensive solutions. For instance, the electrochemical polishing (Ref 36), magnetic polishing (Ref 37), vibratory finishing (Ref 38), barrel finishing (Ref 17, 39), ultrasonic shot peening (Ref 18, 40), and shot peening (Ref 18, 41-44) may be applied for surface treatment of the small-sized and complexly shaped superalloy parts. To finish the large-scale nickel-based alloy components, the shot/cavitation peening, laser peening (Ref 45), ultrasonic peening/finishing (Ref 17, 18, 46), and ball burnishing (Ref 47) can be used in manufacturing processes.

A significant improvement in the surface roughness, as well as the δ and carbide phases instead of γ phases on the untreated surface specimens, were observed after electrochemical polishing with a long duration (Ref 36). The vibratory and barrel finishing resulted in a 10-15% surface hardness increment in the L-PBF-printed IN 718 alloy parts (Ref 18, 38). Kim et al. (Ref 40) confirmed the improvement of the mechanical and tribological properties of the L-PBF-built Fe-Ni-Cr alloy specimens subjected to HIP treatment followed by shot peening. The shot peening led to the formation of high compressive residual stresses in the L-PBF-built IN 718 alloy parts subjected to prior solution annealing and double aging or heat treatment followed by HIP treatment (Ref 44). At the same time, the attempts to use the shot peening surface treatment after prior HIP and heat treatments to improve the surface layer properties of the L-PBF-built complexly shaped superalloy components are virtually absent.

The purpose of this work is to analyze the effects of the thermo-mechanical post-processing on the microstructure, phase composition, bulk/superficial strengthening, subsurface porosity, and surface roughness of the IN 718 alloy turbine blade parts printed by the laser powder bed fusion technology. In particular, the outcomes of excluding homogenization from the standard thermal treatment route and application of shot peening post-processing are under consideration.

2. Experimental Procedure

2.1 Laser Powder Bed Fusion Process Details

The turbine blade test parts (~ 85 mm (X) \times ~ 32 mm (Y) \times ~ 60 mm (Z)) were fabricated by the laser powder bed fusion (L-PBF) process using an industrial Renishaw AM400 additive manufacturing machine (Machineseker, UK) and a nickel-based pre-alloyed IN 718 powder with predominantly spherical shaped particles (over 80% of the particles showed 100% sphericity) and the particle size distribution in a range of 10-55 μ m (Ref 18, 48, 49). The chemical composition of the used powder is presented in Table 1, which meets the specific chemical composition of IN 718 alloy.

The applied L-PBF additive manufacturing system (250 \times 250 \times 300 mm for the X, Y, and Z axis, respectively) was equipped with a ytterbium fiber laser with a maximum power of 400 W CW-M and a galvanometric 3D scanner for laser beam movements (focal spot size of 70 μ m) with a maximum scanning speed of 7000 mm/s. The parts were manufactured in an argon atmosphere using a powder layer thickness of 60 μ m, a scanning speed of 700 mm/s, and a laser power of 200 W

Table 1 Nominal chemical composition of IN 718 powder, in weight percent, wt.%

Ni	Cr	Nb	Mo	Ti	Co	Al	Mn/Si	Cu	C	P/S	O	Fe
50-55	17-21	4.7-5.5	2.8-3.3	0.65-1.15	≤ 1.0	0.2-0.8	≤ 0.35	≤ 0.30	≤ 0.08	≤ 0.015	≤ 0.03	Bal.

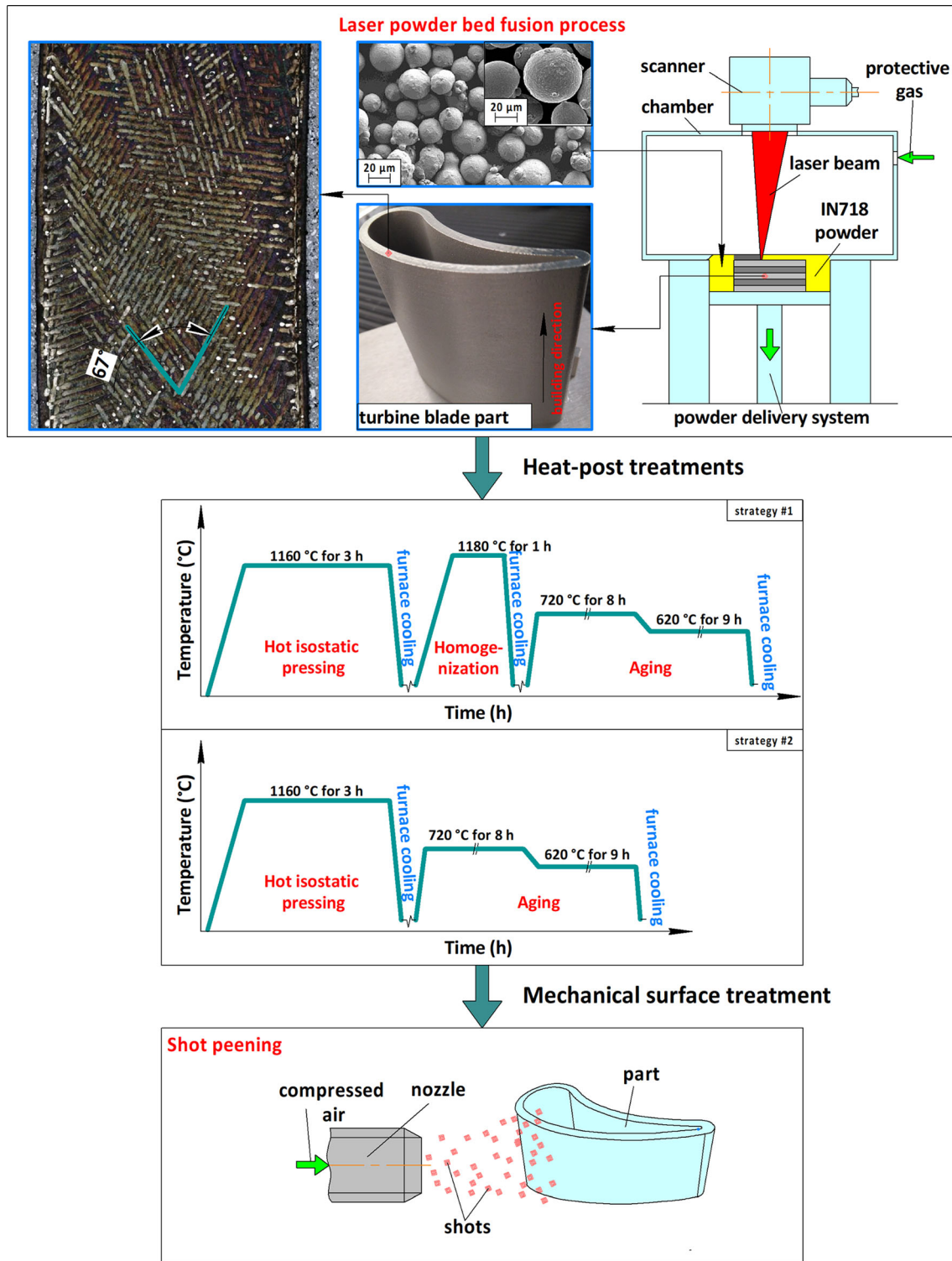


Fig. 1 Schematic illustration of L-PBF process followed by thermo-mechanical post-processing

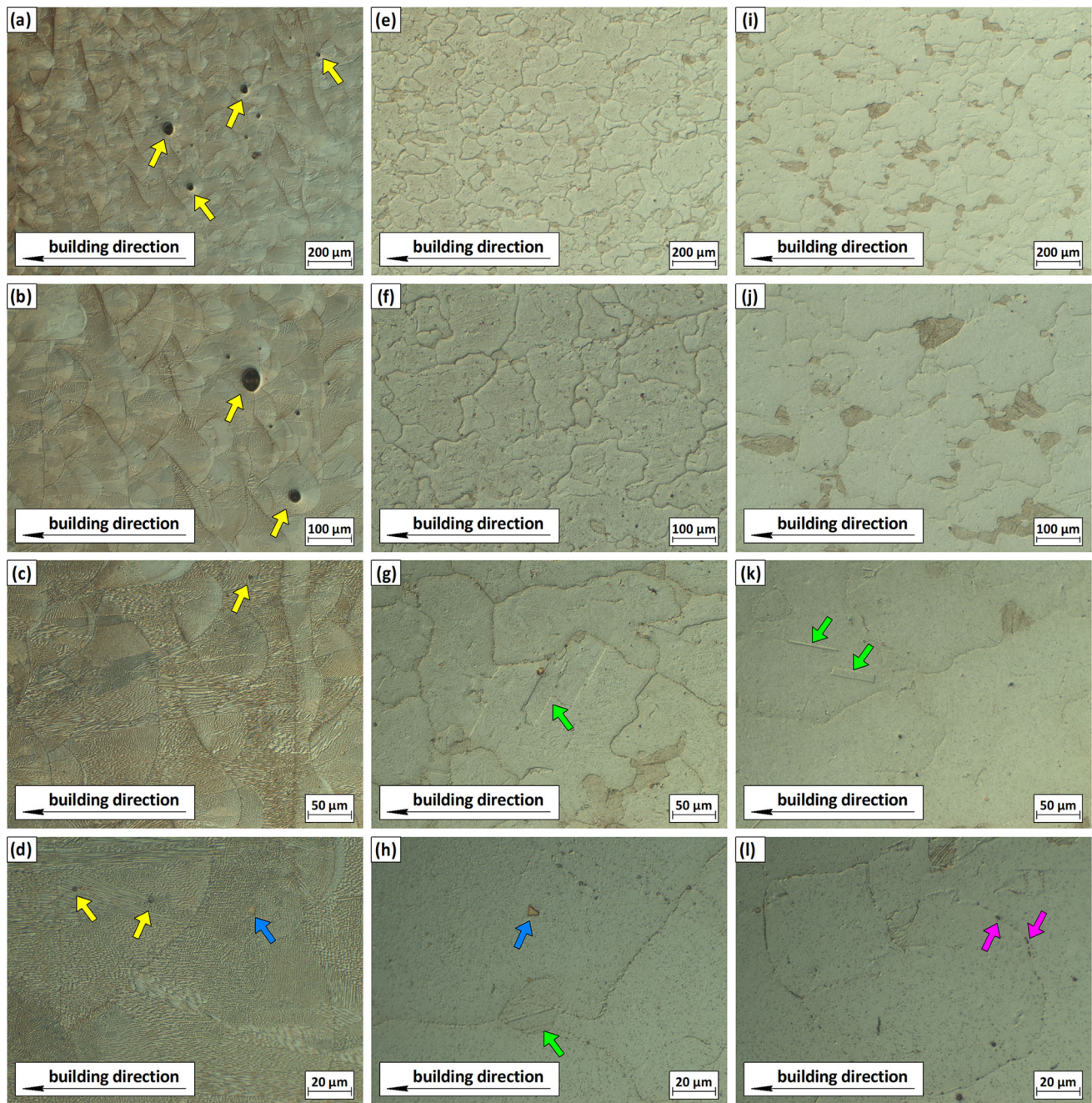


Fig. 2 LOM micrographs of microstructure in the building direction of the LPBF-built (a-d) and HIP+H+A (e-h), HIP+A (i-l) post-processed IN 718 alloy specimens

(Fig. 1). A multidirectional stripe scanning strategy with lines spacing of $80\ \mu\text{m}$ and stripes spacing of $5\ \text{mm}$ was applied when the biaxial laser scanning patterns were rotated by 67° between each powder layer (Ref 41). The QuantAM software was used to program the stripe trajectory parameters. The turbine blade parts were separated from the build platform and further cut/prepared using electric discharge machining. Then

the specimens were subjected to the thermo-mechanical post-processing as shown in Fig. 1.

2.2 Post-processing

2.2.1 Hot Isostatic Pressing. To eliminate the internal porosity and increase the material density, all studied L-PBF-built parts were subjected to the hot isostatic pressing (HIP)

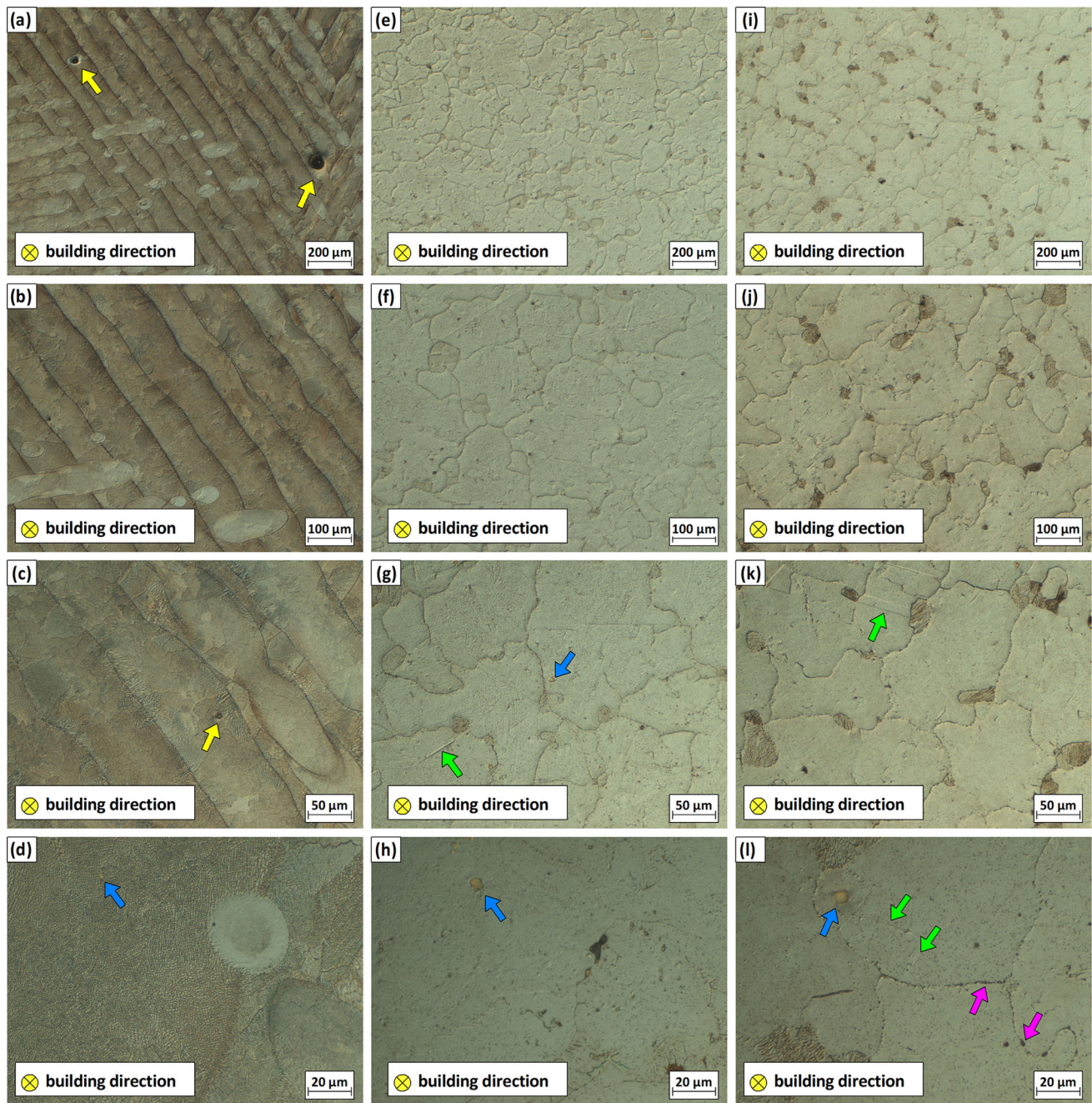


Fig. 3 LOM micrographs of microstructure in the scanning direction of the LPBF-built (a-d) and HIP+H+A (e-h), HIP+A (i-l) post-processed IN 718 specimens

process per ASTM F3055 using a modern hot isostatic press QIH 0.9 x 1.5-2070-1400 MURC (QUINTUS, Sweden) (Ref 42). The HIP treatment consisted of a heating temperature of 1160 °C and an argon pressure of 160 MPa for 3 h (Fig. 1). To increase the cooling rate in the HIP furnace, the forced-convection high-speed cooling of the highly pressurized argon gas was applied inside the pressure vessel during the cooling of the L-PBF-built parts.

2.2.2 Heat Post-processing. The HIP-processed specimens were subjected to a homogenization (H) heat treatment followed by double aging (A) heat treatment (marked as HA or H+A) and single/direct double aging heat treatment (marked as

A). In particular, the homogenization heat treatment of the HIP-processed specimens was carried out at the heating temperature of 1180 °C for 1 hour using an IPSEN T2T vacuum furnace (Fig. 1). The specimens were cooled in the furnace, conducting argon gas streaming. The double aging was carried out using an SNV 80 vacuum furnace at 720 °C for 8 h followed by furnace cooling to 620 °C and holding for 9 h (Fig. 1). The cooling was performed in the furnace to 80 °C in a protective gas (argon).

2.2.3 Mechanical Surface Post-processing. Finally, after HIP followed by various heat treatments, the specimens were deformed by an air blast shot peening (SP) to improve the surface roughness parameters, eliminate the defects on the

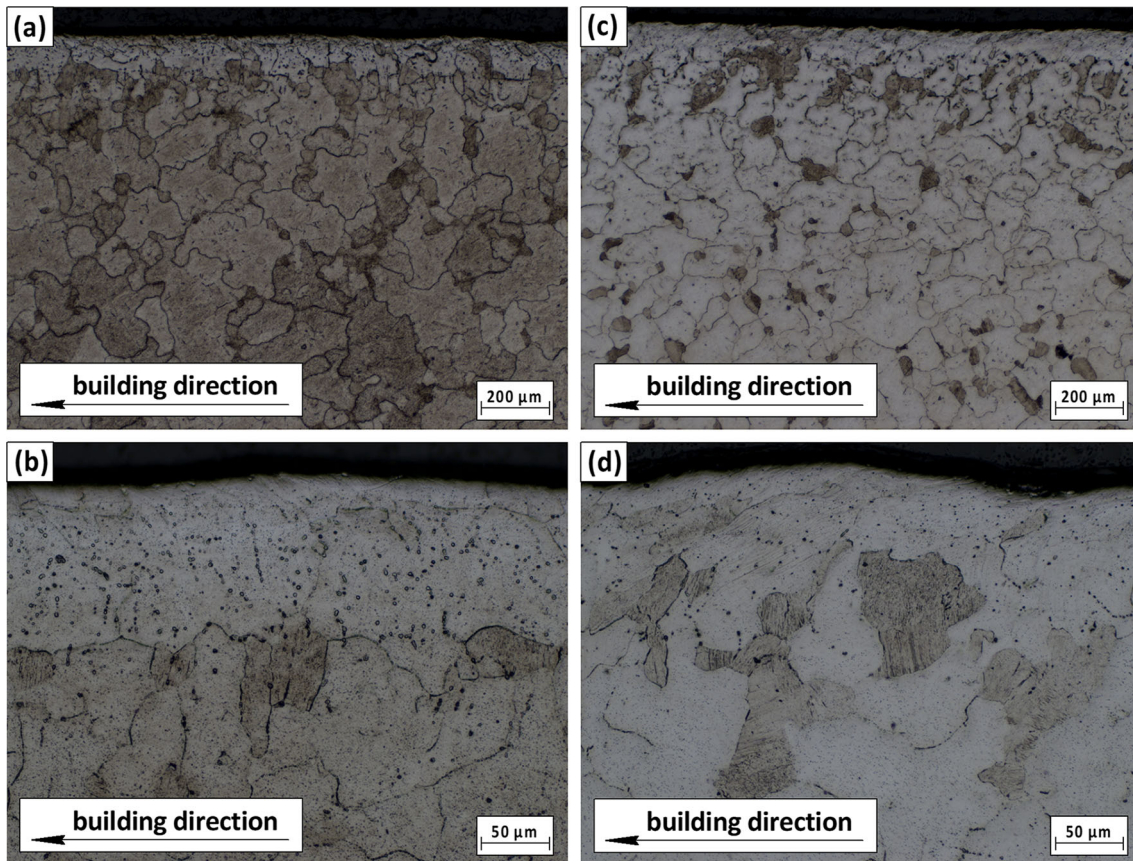


Fig. 4 LOM images of microstructure of the subsurface layer in the building direction of the HIP+H+A+SP (a, b), and HIP+A+SP (c, d) post-processed IN 718 specimens

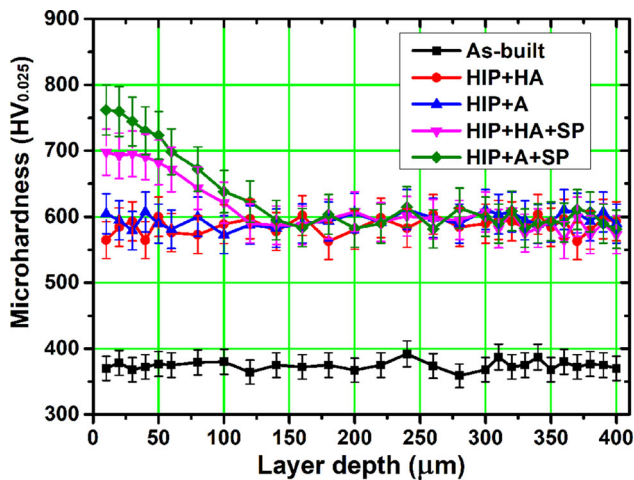


Fig. 5 Microhardness distribution in the building direction of the LPBF-built and HIP+H+A, HIP+A, HIP+H+A+SP, HIP+A+SP post-processed IN 718 specimens

surface, and provide a new surface texture/microrelief, which is known to be beneficial in the enhancement of the surface-related properties. The SP treatment was carried out using a commercial shot peening system (Ref 41). The turbine blade specimens were processed by SP at a peening pressure of 0.55 MPa, a stand-off distance of 15-30 mm, and feed rate of a nozzle of ~ 10 mm/s using steel balls of 0.5 mm diameter (average hardness was 48 HRC), conducting 4-6 passes for a full surface coverage (Fig. 1).

2.3 Specimen Characterization

2.3.1 Microstructural Observation. The turbine blade parts were mechanically cut into vertical (section perpendicular to the fused layers) and horizontal (section parallel to the fused layers) cross-sections and prepared according to a standard metallographic procedure. The specimens were electrolytically etched at the voltage of 2.5 V and current of 0.2 A by a Lucas' reagent consisting of the lactic acid (50 ml), hydrochloric acid (150 ml), and oxalic acid (3 g) for 5-10 s. The bulk and surface microstructures were observed by a LEICA Reichert Polyvar 2 light optical microscope (LOM). The microstructure at high magnification and elemental chemical composition was studied

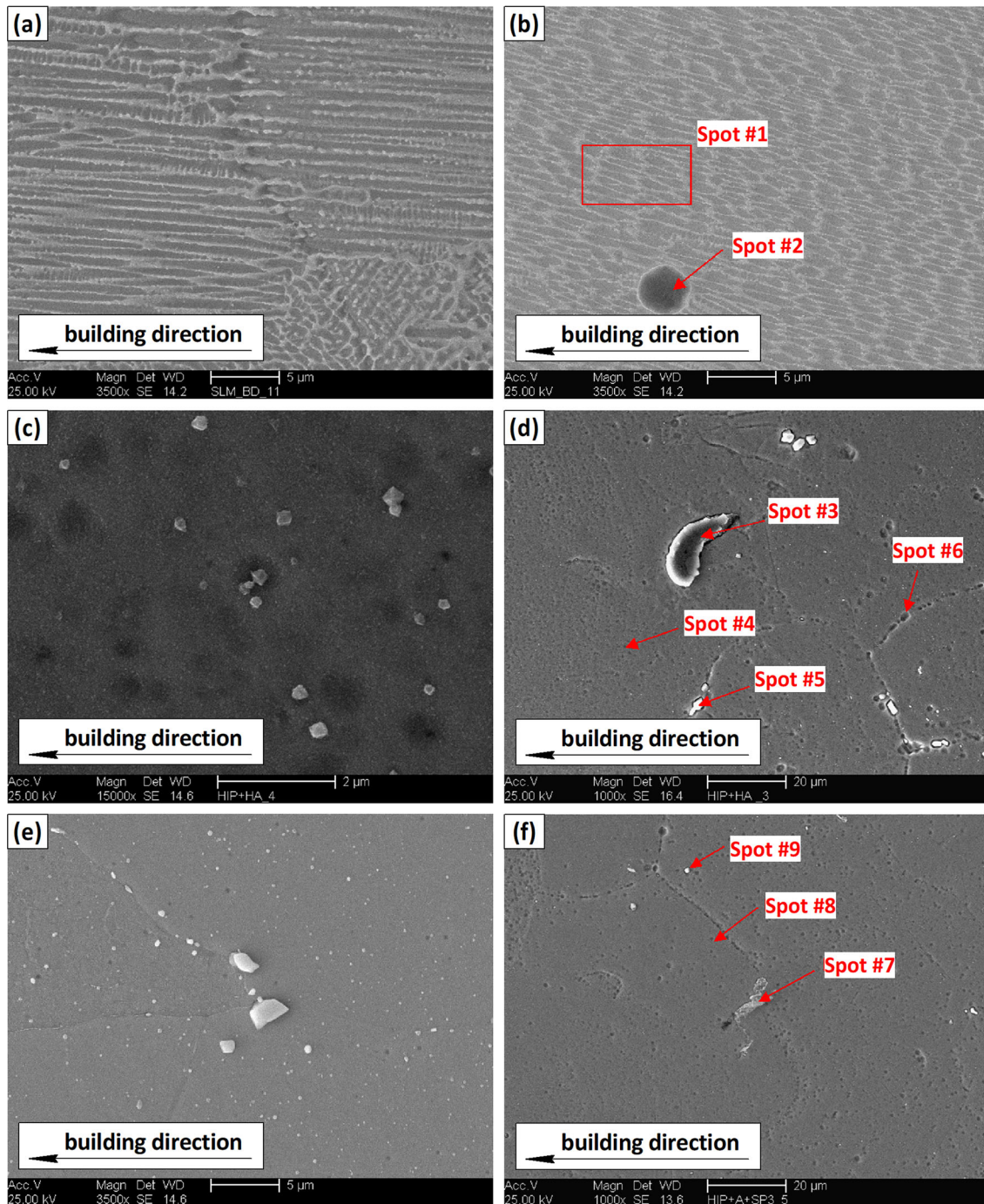


Fig. 6 SEM micrographs of microstructure in the building direction of the LPBF-built (a, b) and HIP+H+A (c, d), HIP+A (e, f) post-processed IN 718 specimens

using an XL 30 ESEM scanning electron microscope (SEM) equipped with an energy-dispersive x-ray spectroscopy (EDS) detector.

The x-ray diffraction (XRD) analysis of the L-PBF-built and post-processed specimens was conducted using a Rigaku Ultima IV diffractometer in a $\text{CuK}\alpha$ -radiation at the voltage of 30 kV, current of 30 mA, and scanning speed of 2 °/min. The peak deconvolution software, OriginPro 9.0 for Windows, was used to complete the XRD peak analysis by applying Gaussian fitting (Ref 41). The residual macrostresses in the subsurface layers were estimated based on a shift in the

diffraction maximum (220) of the SP, HIP, HIP+H+A, HIP+A, HIP+H+A+SP, HIP+A+SP-processed specimens from their positions registered for the LPBF-printed specimen

2.3.2 Hardness and Roughness Measurements. The microhardness depth profiles in the sample cross-sections were obtained in the building direction using a tester Leica VMHT with a Vickers indenter loaded by 0.025 kg ($\text{HV}_{0.025}$) and the dwell time of 15 s. The scatter of the experimental data did not exceed by 5%.

The surface roughness parameters of each specimen were evaluated based on the 2D surface parameters (R_a , R_p , R_v , and

Table 2 Chemical composition of the IN 718 alloy features, in wt.%

	State	Spectrum markings	Feature	C	O	Al	Ti	Ni	Cr	Fe	Nb	Mo
Fig. 6b	L-PBF-built	#1	γ -phase	4.21	0.39	0.43	1.05	51.91	16.5	16.4	5.81	3.2
		#2	pore	9.70	16.1	18.29	5.29	22.23	10.41	11.51	2.26	1.16
Fig. 6d	HIP+H+A	#3	NbC	7.2	0.3	0.33	0.93	24.99	14.24	12.70	36.28	3.05
		#4	γ -phase	3.86	0.3	0.47	0.65	53.32	16.79	15.40	5.93	3.28
		#5	NbC, TiC	8.83	0.11	0.35	12.38	16.28	7.84	7.40	43.19	2.63
		#6	γ'' -phase	5.40	0.33	0.42	1.16	47.37	9.99	10.72	23.44	3.17
Fig. 6f	HIP+A	#7	NbC, TiC	8.24	0.32	1.34	5.91	14.05	15.23	15.74	39.21	0.14
		#8	γ -phase	3.21	0.2	0.43	0.96	53.14	16.96	16.69	5.19	3.22
		#9	NbC	7.05	0.19	0.37	1.21	11.75	16.06	16.39	43.85	3.12

R_z) of the profiles obtained using a 3D Taylor Hobson Form Talysurf 120 surface contact profilometer. For each specimen, eight measurements were taken at different locations along the X and Y axes using a roughness filter cut off 0.8 mm. The scatter of the experimental data did not exceed by 5%.

3. Results and Discussion

3.1 Microstructure

3.1.1 LOM Observations. The evolutions of the microstructure in the building (longitudinal-section) and scanning (cross-section) directions of the L-PBF-built IN 718 alloy turbine blade caused by the HIP treatment followed by heat treatments are presented in Fig. 2 and 3, respectively. The macrostructure of the L-PBF-built alloy is characterized by the overlapped semi-circular melt pool boundaries/patterns in the building direction (Fig. 2a-c), while the boundaries of laser passes are observed in the scanning direction (Fig. 3a-c). The melt pool width is ranged from 60 to 120 μm . Figure 3a shows the used laser scanning strategy, which includes a $+67^\circ$ hatch rotation between built layers. It is well-known that the fine columnar-shaped randomly oriented grain (dendritic) microstructure with randomly oriented grains and cuboidal interdendritic precipitates are formed when a layer-by-layer building with rapid cooling of the melt pool is used (Ref 14, 34, 41). In the longitudinal section, the dendritic microstructure of the L-PBF-built IN 718 alloy specimen mainly consists of elongated colonies of cells across multiple layers, which grow epitaxially from the substrate into the direction determined by the heat flow direction (Fig. 2c, d). The transversely cut dendritic cells can be observed in Fig. 3(d). The spherical or shrinkage pores are indicated by yellow arrows in Fig. 2(a-d), 3(a, c).

Application of the HIP treatment combined with heat treatments lead to the formation of homogeneous/equiaxed grain microstructure with precipitations of secondary phases appearing along the grain boundaries instead of the dendritic cellular microstructure (Fig. 2e-l, 3e-l). The final microstructure of the HIP+H+A-processed specimen (Fig. 2e-h, 3e-h) is almost similar to that of the HIP+A-processed specimen (Fig. 2i-l, 3i-l). As the temperature used at HIP and homogenization treatments was high enough (1160-1180 $^\circ\text{C}$), the interdendritic areas mainly consisted of Nb-rich Laves and δ phases were almost dissolved after HIP or HIP+H processes (Ref 29, 34, 50, 51). Only some portion of niobium/titanium carbides left on the formed grain boundaries (indicated by blue arrows in Fig. 2l, 3l) after the dissolution of the interdendritic

areas observed in the L-PBF-built microstructure. Notice, that the grain size of γ -matrix appears slightly larger after additional homogenization (HIP+H) as compared to that after a single HIP process. It seems that the longer the high-temperature holding, the lower the quantity of the NbC carbides, and thus, the lower obstacles left to the grain growth in the case of the HIP+H+A-processed sample. Also, TiC carbides (indicated by pink arrows in Fig. 2h, 3g, h, l) and annealing twins (indicated by green arrows in Fig. 2g, h, k, 3g, k, l) were appeared in the γ -phase matrix. Double aging heat treatment of both the HIP+H and single HIP-processed specimens results in precipitation of fine γ' and γ'' strengthening particles into the γ -phase matrix. Contrary to some literature data (Ref 52), neither needle-like δ phase nor Laves precipitates were found due to high enough HIP and homogenization temperatures, which are higher than the reported dissolution temperatures for these phases (Ref. 29, 50, 51, 53). It was recently revealed that the combination of HIP treatment with direct double aging led to a remarkable improvement of the creep behavior of the studied alloy (Ref 25, 37). Moreover, the equiaxed grain structures contribute to better corrosion resistance (Ref 43).

The surface severe plastic deformation exerts a two-fold influence on the HIP+H+A and HIP+A specimens of IN 718 alloy. Firstly, it eliminates all surface defects, such as signs of the laser passes, spattering powder particles, needle-like tips, and deep pits (Fig. 4). Secondly, it results in the grains' reshaping in the subsurface layers: the thickness of the near-surface grains gets smaller as the grains become elongated along the shot-peened surface. Despite some deformation-induced temperature increase (Ref 54), the phase compositions of the HIP+H+A+SP and HIP+A+SP post-processed specimens appear to be similar to those of the heat-processed specimens and will be considered in detail below using SEM and XRD data.

The microhardness depth distribution in the near-surface layers (longitudinal-section) before and after post-processing is shown in Fig. 5. After the application of the HIP+H+A and HIP+A heat post-processing, the microhardness of the L-PBF-built specimen was increased by about 50%. This is because the HIP followed by double annealing treatments induced the nucleation and growth of γ' and γ'' phases, providing the precipitation hardening effect. Compared to the surface microhardness (HV) of the HIP+H+A and HIP+A post-processed specimens, the SP-produced surface hardness was further increased by $\sim 25\%$, forming the hardening depth of 120-140 μm . The reason for this strain-induced hardening of the surface naturally relates to the increased dislocation density, their rearrangement, and subgrain formation (Ref 41, 43, 44). However, the combined HIP+A+SP regime produces a slightly

higher increment in the microhardness (~ 760 HV_{0.025}) as compared to that of the combined HIP+H+A+SP regime (~ 700 HV_{0.025}) (Fig. 5). This can be attributed to the different grain sizes of the γ -phase matrix and different volume fractions and sizes of the precipitated phases HIP+H+A (Fig. 4a) and HIP+A (Fig. 4c) post-processed specimens. As a result, these differences may affect the hardening rate at the severe SP treatment.

3.1.2 SEM Observations. The corresponding weight percentage of the chemical composition of the specific particles in the building direction for the L-PBF-built (indicated in

Fig. 6b) and HIP+H+A (indicated in Fig. 6d)/HIP+A (indicated in Fig. 6f) heat post-processed IN 718 alloy specimens obtained by the EDS technique is given in Table 2. Spectrum #1 represents the γ -phase matrix of the L-PBF-built alloy. It can be seen that a pore in the L-PBF-built specimen contains oxide fragments (spectrum #2). In the heat post-processed specimens, the particles of niobium carbide (spectrums #3 and #9) contain a similar weight percentage of constituent elements with about 7-8% C, 36-39% Nb, and other elements contributing from the surrounding matrix. Additionally, the MC-carbide particles

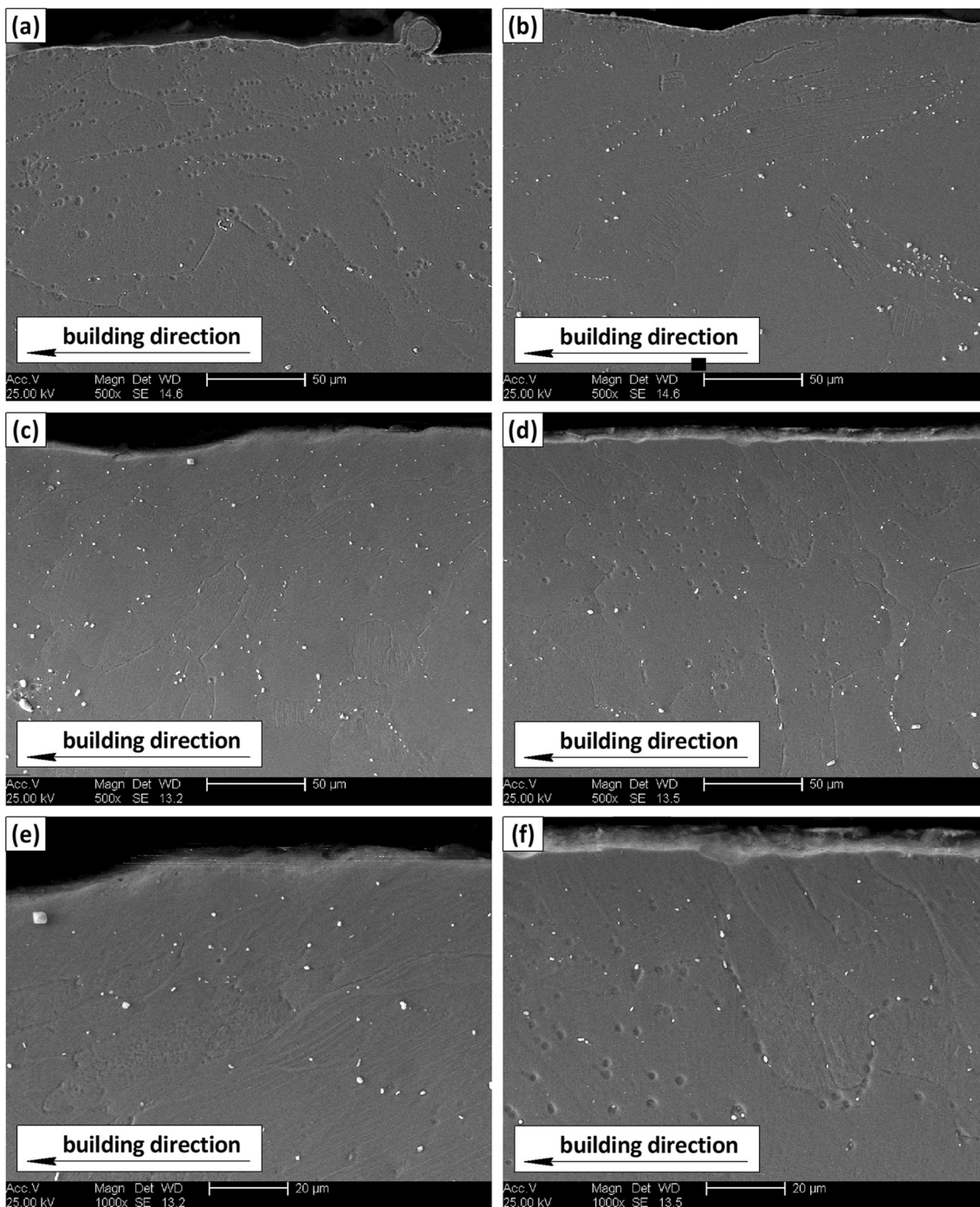


Fig. 7 SEM micrographs of microstructure of the near-surface layer in the building direction of the HIP+H+A (a), and HIP+A (b), HIP+H+A+SP (c, e), and HIP+A+SP (d, f) post-processed IN 718 specimens

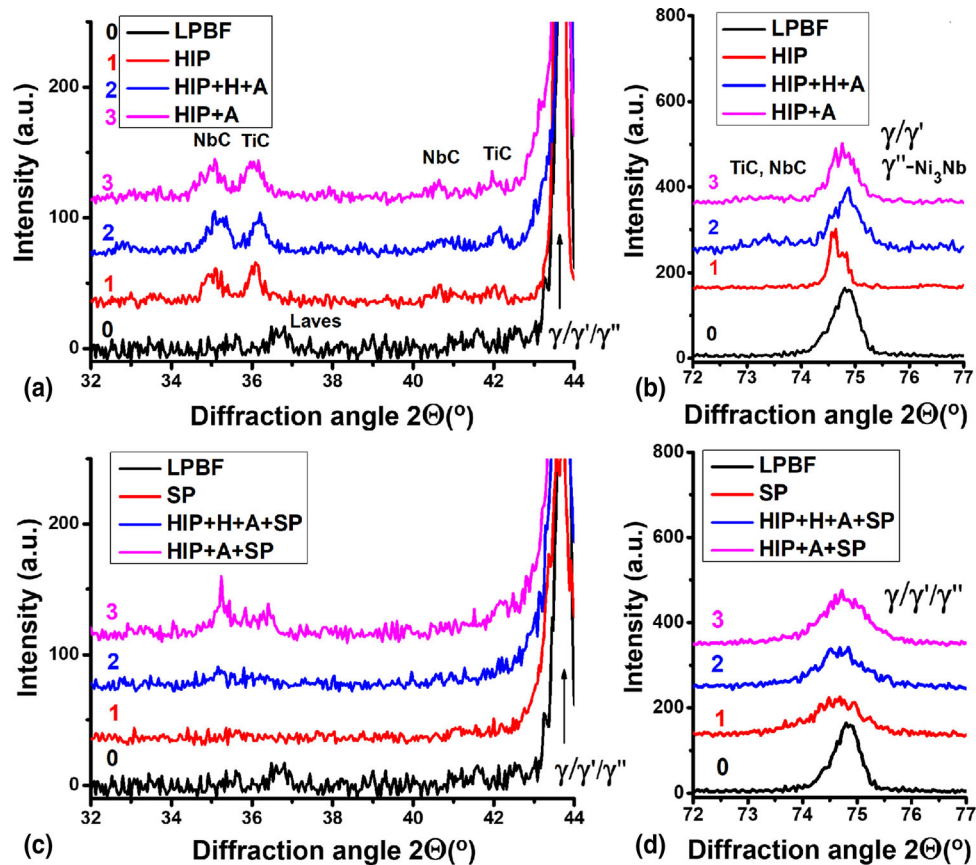


Fig. 8 Fragments of XRD spectra of the LPBF-built and HIP+H+A, HIP+A (a,b), SP, HIP+H+A+SP, and HIP+A+SP (c,d) post-processed IN 718 specimens

(spectrums #5 and #7) are characterized by a higher amount of both Nb and Ti elements indicating their composite structure (NbC/TiC) like that reported in (Ref 55-59).

Additionally, the SEM observations of the subsurface micrographs in the longitudinal-section (building direction) shown in Fig. 7(c-f) also confirm significant surface plastic deformation of the subsurface layer regardless of the prior heat treatment used. The grains are seen to become inclined to the specimen surface (Fig. 7e) as compared to the heat post-processed specimen microstructure (Fig. 7a). Work by Ardi (Ref 44) confirmed that average grain size in the H+HIP heat-processed specimens was reduced by SP due to severe plastic deformation.

3.1.3 XRD Analysis. Figure 8 shows the fragments of x-ray diffraction (XRD) patterns of the studied specimens of IN 718 alloy in the L-PBF-built and HIP-processed states and after various thermal treatments (Fig. 8a, b) and shot peening (Fig. 8c, d). It is seen that in comparison with L-PBF-built specimen containing mainly γ (fcc solid solution), γ' ($\text{Ni}_3(\text{Ti}, \text{Al})$), and Laves phases. Following HIP at 1160 °C and compressive load results in the dissolution of Laves and other Nb-rich phases and appearance of (Nb,Ti)C carbides (which dissolution temperatures are higher (Ref. 51)), and additional XRD peaks related to them appear (Fig. 8a). These observations correlate well both to our SEM data (Fig. 6) and to the literature data (Ref 29, 41, 55, 56, 60, 61). It is well-known that as compared to the conventional casting methods, the LPBF

process provides relatively quick solidification and some cyclic reheating of the sequentially added layers, and the built material usually contains cellular structure (dendritic/interdendritic areas) with residual defects (pores, dislocations, twins) and residual stresses (Ref 29, 51, 62). Thus, the observed XRD peak of the LPBF-built sample is rather broad (Fig. 9a).

The HIP process used for the dissolution of the Laves facilitates supersaturation of the fcc solid solution with the Nb element. Therefore, the XRD peak of the γ phase becomes shifted to a lower diffraction angle (Fig. 9b). Additionally, the widths of the XRD peak and deconvoluted sub-peaks are much lower than those of the LPBF sample due to thermal stress-relieving. At the same time, the intensity of the sub-peaks related to γ'/γ'' phases is increased after HIP, indicating the increase in the volume fractions of these phases (Fig. 9b). This observation correlates to the literature data regarding the phase composition changes in the HIP-processed IN718 alloy obtained by neutron diffraction (Ref 63). Notice also the increased intensity of the peaks related to the carbides (Fig. 8a, 9, 10).

Following homogenization (H) and aging (A) processes lead to a substantial increase in the volume fraction of γ' / γ'' phases, which manifests itself by the increased integral intensity of appropriate sub-peaks of this phase (Fig. 9c, d). Comparison of the angular positions of the (220) cumulative peaks for the L-PBF-built and heat-treated specimens (Fig. 8b), which are composed by the sub-peaks related to three phases— γ , γ' , γ'' , allows assessing the changes in the lattice

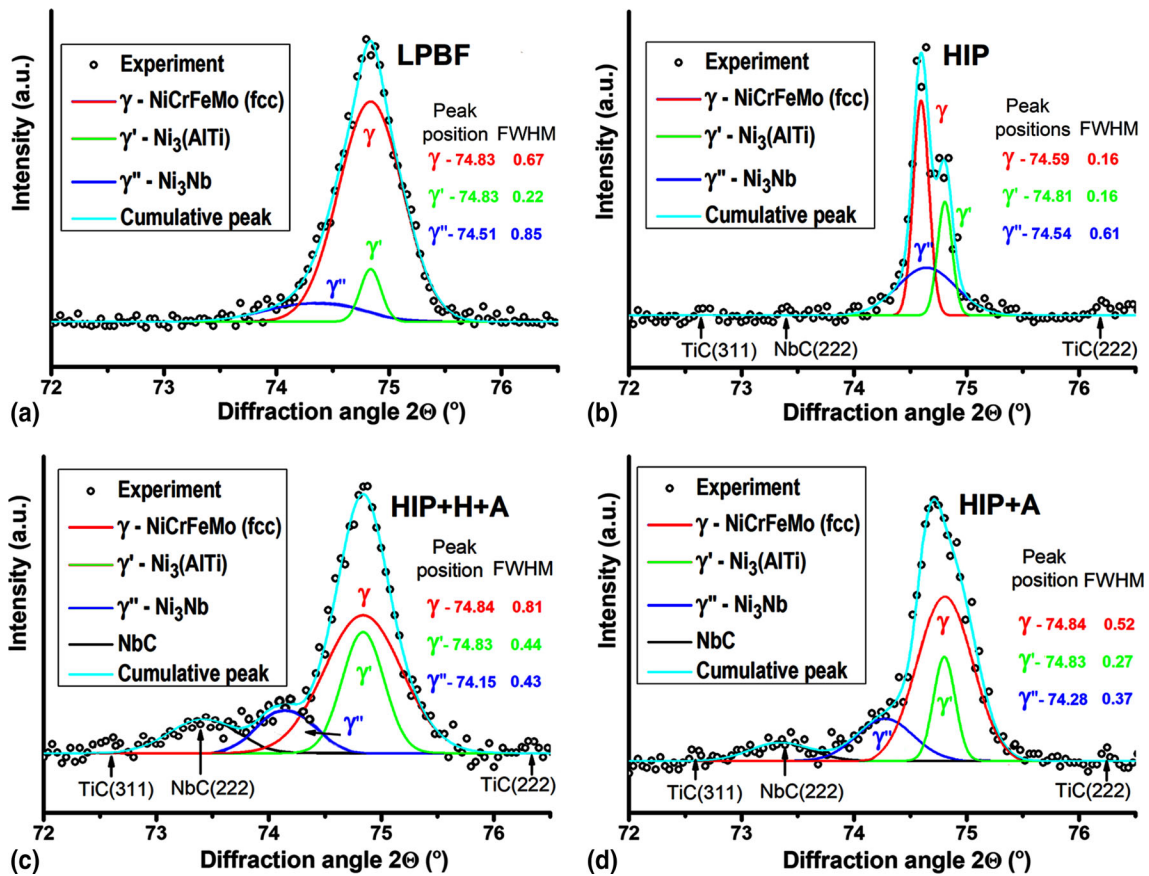


Fig. 9 Deconvolution of (220) XRD peak of the LPBF-built (a), and HIP (b), HIP+H+A (c), and HIP+A (d) post-processed IN 718 specimens

parameters of the appropriate phases. As seen, the (220) peak registered for L-PBF-built specimen is asymmetrical due to the dendritic microstructure with varying lattice parameters of the γ phase variants situated in the dendrites and interdendritic areas. The HIP process shifts the (220) peak to the lower diffraction angles indicating the increased Nb content in the γ solid solution caused by the enhanced dissolution of dendrites (Laves) formed during L-PBF manufacturing. Further homogenization and aging lead the (220) γ sub-peak to be shifted to higher diffraction angles again that can be provoked by the aging-promoted precipitation of the Nb containing phases (γ' (Ni₃(Al,Ti)), γ'' (Ni₃Nb) and (Nb,Ti)C carbides) accompanied with the Nb depletion of the γ solid solution (the decrease in the γ lattice). Additionally, the higher the Nb content and the more uniform Nb distribution, the higher the volume fractions and the smaller the size of the γ'' and γ' precipitates can be formed (Ref 51, 57, 62). Our experimental data also confirm this statement: considering the broader sub-peaks of the γ'' and γ' phases, they are expected to be of smaller size in the case of the HIP+H+A regime. The volume fractions of the NbC/TiC carbides are also seen to be increased after annealing, and this increase is higher for the case of the HIP+H+A regime (Fig. 9c) as compared to the HIP+A regime (Fig. 9d).

Application of the SP process to the specimens that underwent various thermal treatments results in a significant broadening of diffraction peaks owing to the SP-induced severe plastic deformation of the subsurface layers (Fig. 8d). The

(220) peaks are shifted to the lower diffraction angles. However, another reason for this shift should be considered in this case—the SP-induced severe plastic deformation is clear to result in the formation of compressive residual stresses, which can manifest themselves by such a shift of the diffraction peaks. It is seen that the previously heat-treated specimens, which are characterized by higher hardness, demonstrated a lower shift of the (220) peak owing to the fact that these samples, which were precipitation strengthened during two-step aging, are less prone to straining, and thus, residual stresses of a lower magnitude can be formed.

To assess the phase compositions of the L-PBF-built and thermo-mechanically post-processed specimens, the deconvolution procedure was applied to the cumulative diffraction peaks (220). The peak deconvolution software, OriginPro 9.0 for Windows, was used to complete the XRD peak analysis by applying Gaussian fitting (Ref 41, 61, 64). Figure 9 shows the (220) peaks registered for the L-PBF-built and the HIP, HIP+H+A and HIP+A post-processed specimens after their deconvolution to three/four peaks related to (220) γ , (220) γ' , (220) γ'' , and (222) NbC phases. Such detailed analysis of the diffraction maximums allows to evaluate the evolution of the considered phases during HIP and further thermal treatments. It is seen that HIP causes significant thinning of the diffraction sub-peaks related to γ and γ' phases, while the γ'' -phase-related sub-peak remains broadened. This situation can be explained by the dissolution of the dendrites (Laves) supplemented by the

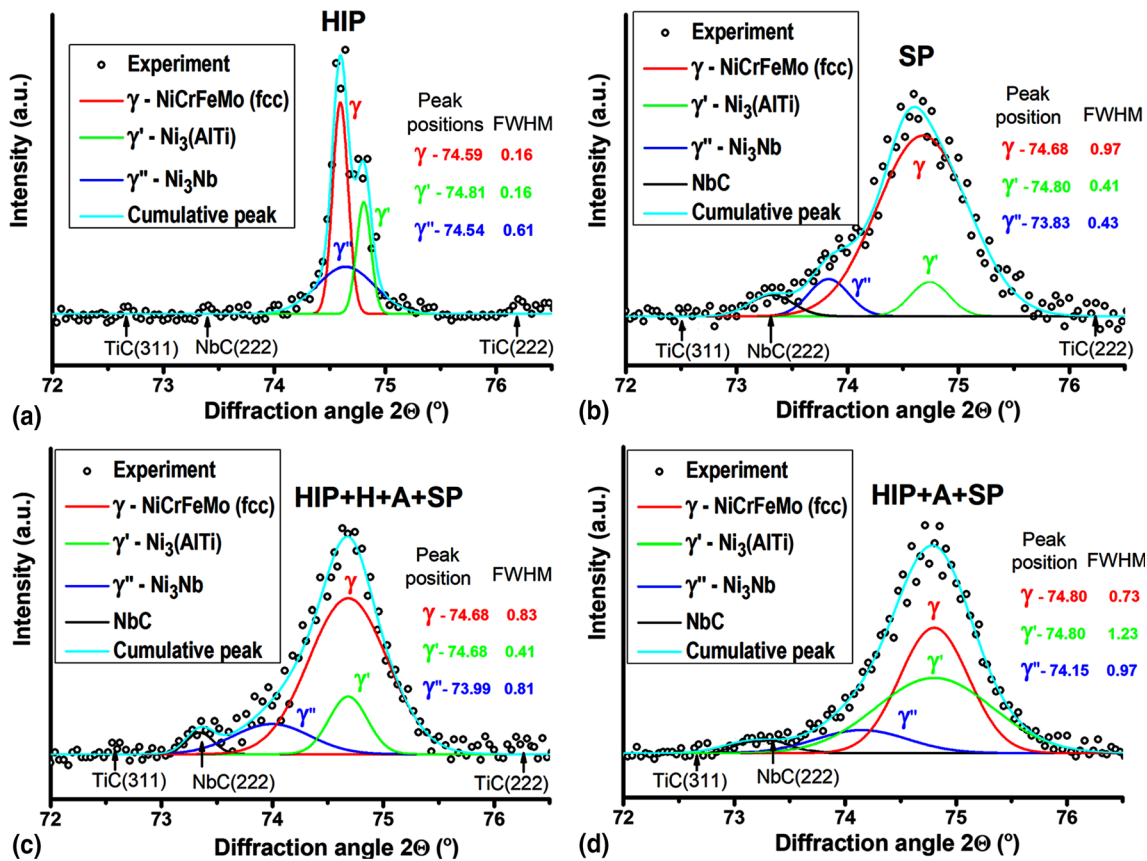


Fig. 10 Deconvolution of (220) XRD peak of the HIP (a), SP (b), HIP+H+A+SP (c), and HIP+A+SP (d) post-processed IN 718 specimens

redistribution of Nb between the γ solid solution and γ'' phases retaining on the grain boundaries formed instead of the dissolved the interdendritic areas. During HIP, the newly formed γ'' phase nanoprecipitates have different orientations, which produce a broadened diffraction sub-peak (Ref 53, 59, 61, 65-67). Following homogenization and aging (the 'HIP+H+A' sample) result in a further broadening of the γ and γ'' phase sub-peaks and in the increase in the intensity of NbC/TiC peaks (Fig. 9c). In the case of the aging process carried out just after HIP (without intermediate homogenization), the FWHM values of the γ and γ' sub-peaks are observed to be slightly lower (Fig. 9d) in comparison with the previous case (Fig. 9c). The phase formation registered in this study well correlates to the reported 'continuous-cooling-transformation' diagram and 'time-temperature-transformation' diagram of IN 718 alloy in the homogenized (1180 °C) and/or solution-annealed (1149 °C)/water-quenched conditions (Ref 56-59).

Similar deconvolution of the (220) XRD peaks was performed to analyze the changes in microstructure and phase compositions of the surface layers of the heat-treated specimens after shot peening (Fig. 10). It is seen that in comparison with the HIP-processed sample (Fig. 10a) the SP treated sample still contains the same phases, but the registered peaks are significantly broadened (Fig. 10b), and the highest broadening (6 times) is registered for the γ -phase sub-peak. The same but less pronounced trend is observed for the heat-treated and SP-processed samples (Fig. 10c, d). The 5.2 and 4.5 times increase

in FWHM is, respectively registered for the HIP+H+A and HIP+A-processed samples. It is of interest that the volume fraction of the NbC/TiC carbides remains almost unchanged for both the HIP+H+A and HIP+A post-processed samples (Fig. 10c, d). The observation of NbC/TiC carbides correlates to the phase composition of the forged Inconel 718 alloy (Ref 68). It is of importance that the deconvoluted diffraction sub-peaks related to all phases are significantly broadened. It is especially related to the sub-peak of the γ phase. Such broadening is naturally induced by the deformation-induced formation of sub-grains and/or lattice micro-strain increase.

3.2 Bulk Defects

The bulk defects (cracks, incomplete fusion holes, and microporosity) of the L-PBF-printed IN 718 specimens were evaluated in both the longitudinal-section (building direction) and cross-section (scanning direction) using a Leica MEF4A light optical microscope. The average residual porosity in the near-surface layer at a depth of $\sim 50 \mu\text{m}$ was statistically estimated using Image J152 software.

The L-PBF-built turbine blade parts are characterized by a high area fraction of the pores, especially in the near-surface layers (Fig. 11) that determine the relative density of $\sim 99.848\%$ (Fig. 12). These observations correlate well with the literature data (Ref 23, 50). Application of prior HIP treatment eliminated almost all micropores in the L-PBF-printed IN 718 turbine blade parts, providing a high density of

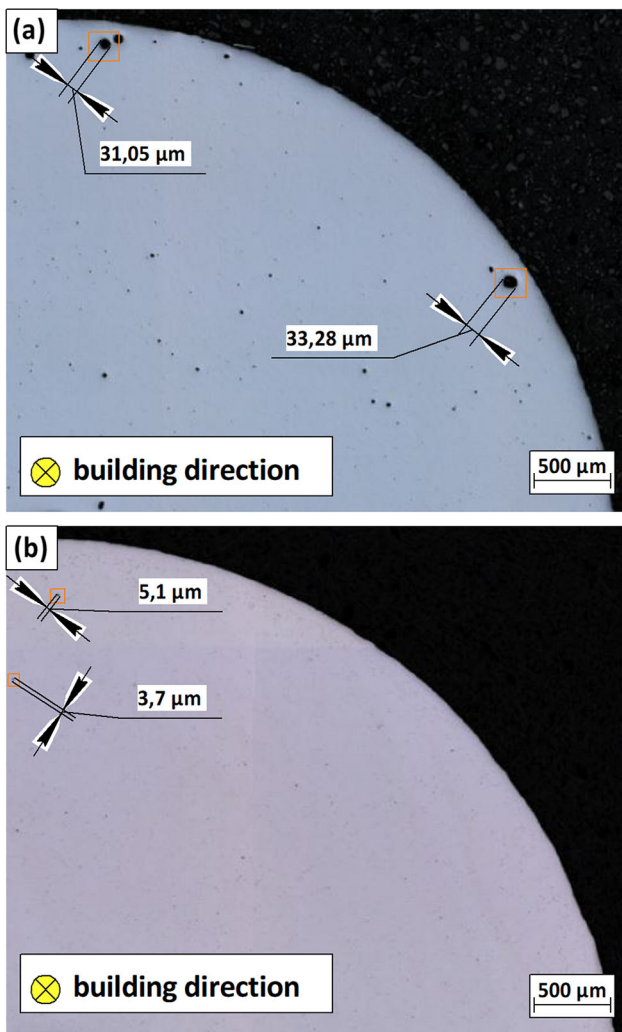


Fig. 11 LOM images of the LPBF-built turbine blade part (a) and after combined thermo-mechanical treatment (b)

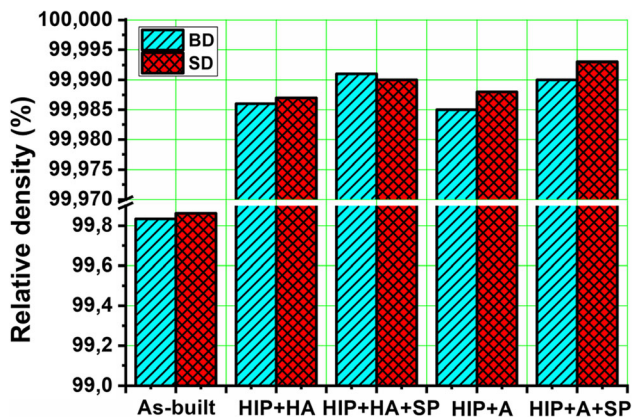


Fig. 12 Relative density in the building (BD) and scanning (SD) directions of the LPBF-built and HIP+H+A, HIP+H+A+SP, HIP+A, HIP+A+SP post-processed IN 718 specimens

the alloy ($\sim 99,986\%$) (Ref 69). It should also be noted that the HIP process cannot eliminate all bulk defects due to trapped argon gas from the L-PBF process (Ref 26). For the sake of example, several small pores observed in the combined thermo-

mechanical post-processed specimen are presented in Fig. 11b. It should also be noted that the SP process slightly increased the material density ($\sim 99,992\%$) in the near-surface layers as compared to the HIP+H+A and HIP+A post-processed samples.

3.3 Surface Roughness

The surface roughness and waviness profiles of the side surfaces of the L-PBF-printed and post-processed turbine blade specimens are presented in Fig. 13. It is well-known that the surface microrelief/texture of the L-PBF-printed parts contains various manufacturing defects, such as signs of the laser passes, balling formation, partially melted powder particles or spattering powder particles, and even open pores (Ref 18, 70). As a result, the L-PBF-printed and heat-processed specimens are rough and have average surface roughness from $\sim 3,5$ to $\sim 5 \mu\text{m}$.

In general, it can be seen that the surface roughness/waviness profiles did not change after the combined HIP+H+A and HIP+A heat-treatments conducted under vacuum (Fig. 13b, c). It is of interest that the magnitudes of the surface roughness profile peaks height (R_p parameter) are much higher than the magnitudes of the surface roughness profile valleys/pits depth (R_v parameter) (Fig. 14). The maximum height of the roughness profile (R_z parameter) is about $25 \mu\text{m}$. As a result, the high surface roughness magnitudes coupled with surface defects (especially open pores and partially melted powder particles) are often undesirable for critical applications of the L-PBF-built nickel-based alloy components widely used in the aerospace industry because such rough surfaces may facilitate the early nucleation of fatigue cracks.

Application of the SP treatment allows smoothing surface profiles of the heat-processed specimens, providing the same roughness profile peak height and roughness profile valley depth (Fig. 13). At the same time, irregular surface microrelief is formed on the peened surfaces owing to the overlapping dimples/pits introduced through collisions of the hard shot media and the workpiece surface (Ref 41, 44). The average surface roughness was registered to be $1,9 \mu\text{m}$ for HIP+H+A+SP-processed specimen and $1,84 \mu\text{m}$ for HIP+A+SP-processed specimen (Fig. 14). Compared to the L-PBF-printed specimens, the R_z roughness parameter was diminished from ~ 25 to $\sim 13 \mu\text{m}$ after combined thermo-mechanical post-processing. The reduction of the valley depth values of surface roughness profile by shot peening may also enhance the corrosion resistance of the heat post-processed IN 718 alloy turbine blade (Ref 41).

Currently, the SP treatment is a highly effective technique that is mainly used to improve the surface finishing and increase the strength of the complexly shaped external surface of the 3D-printed metal parts in the aerospace industry. The SP post-processing results in similar or even better surface quality in comparison with the laser shock peening or submerged laser peening, cavitation peening, barrel finishing, etc. (Ref 18).

4. Conclusions

The turbine blade test IN 718 alloy parts were printed by the 3D laser powder bed fusion technology. To improve both the structure and surface quality in the L-PBF-built heat-resistant

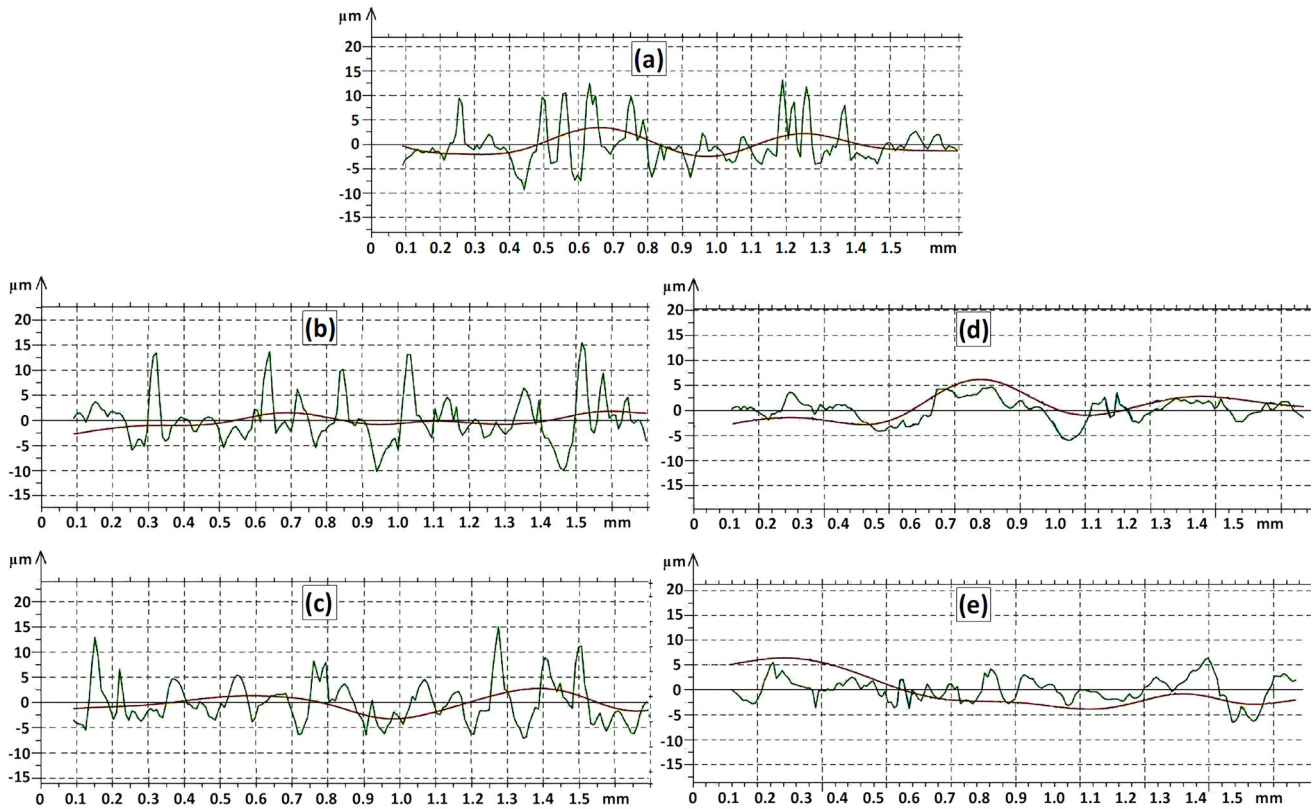


Fig. 13 Surface roughness and waviness profiles of the LPBF-built (a) and HIP+H+A (b), HIP+A (c), HIP+H+A+SP (d), and HIP+A+SP (e) post-processed IN 718 specimens

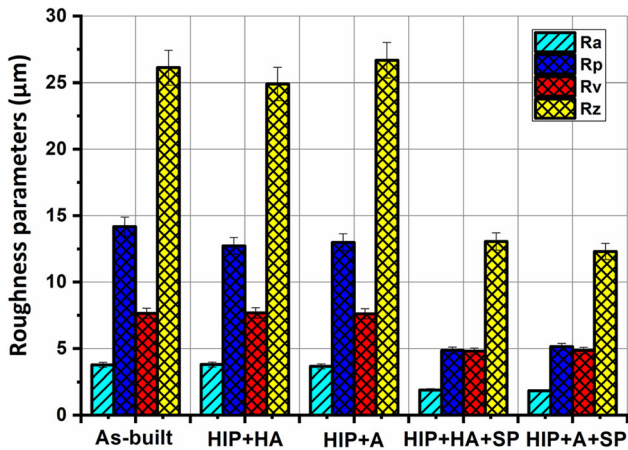


Fig. 14 Surface roughness parameters of the LPBF-built and the LPBF-built and HIP+H+A, HIP+A, HIP+H+A+SP, HIP+A+SP post-processed IN 718 specimens

alloy parts, post-printing thermal-mechanical treatments were applied. The obtained results allow drawing the following conclusions:

(1) The L-PBF-built IN 718 alloy was observed to be consisted of a dendritic microstructure with Nb, Mo and Ti segregated in Laves phase and carbides along the cellular boundary and interdendritic region, while the volume fractions of γ' or γ'' precipitates were small.

- (2) HIP at 1160 °C for 3 h followed by 1 hr homogenization (1180 °C) resulted in the partial dissolution of dendrites and Laves phase, the formation of NbC/TiC carbides as well as the subsequent formation of the γ' and γ'' precipitates during two-step aging (720 C for 8 h followed by 620 C for 8 h). The hardness of the L-PBF-built IN 718 alloy was significantly increased after the two-step aging achieving the highest value of ~ 600 HV after both 'HIP+H+A' and 'HIP+A' processes due to the complete dissolution of Nb followed by the precipitation strengthening caused by the formation of a greater amount of finer γ''/γ' precipitates with more uniform distribution.
- (3) SP leads to the deformation hardening of the subsurface layer caused by both the dislocation activity: (i) sequential redistribution of dislocations, formation of the dislocation cells, and increase in the cells' misorientations (subgrains formation) cause the work-hardening; (ii) mutual interaction between the moving dislocations and fine second phase (γ' , γ'' , and NbC/TiC) particles is responsible for the Orowan's strengthening. The surface microhardness of the L-PBF-built specimen was similarly increased by 25% after shot peening for the specimens that underwent both combined thermo-mechanical HIP+H+A+SP (overall hardening by 78.9% as compared to the L-PBF state), and HIP+A+SP (by 95.3%) post-processing, providing the hardening depth of 120-140 μm .
- (4) The overall reduction in R_a roughness parameter was about 50% after the combined thermo-mechanical HIP+H+A+SP and HIP+A+SP post-processing. In each

case, the final Ra roughness parameter was less than $2\ \mu\text{m}$.

- (5) Considering very similar phase compositions and hardness magnitudes for the HIP+H+A and HIP+A-processed samples, on the one hand, and the possibility to decrease the overall processing consumables in the case of the HIP+A-processed sample, on the other hand, the HIP+A process can be suggested as a trade-off treatment for the IN 718 alloy supporting high enough strength and relatively low time/energy consumables.

Acknowledgments

This work was partially supported by the DAAD program (Grant Number 91695844) and the Ulam NAWA program (Grant Number BPN/ULM/2021/1/00153). The authors would like to thank O. Stamann and S. Faust (Otto von Guericke University Magdeburg, Germany) for the support provided with the surface morphology and roughness measurements.

References

1. S. Sanchez, P. Smith, Z. Xu, G. Gaspard, C.J. Hyde, W.W. Wits, I.A. Ashcroft, H. Chen and A.T. Clare, Powder Bed Fusion of Nickel-Based Superalloys: A Review, *Int. J. Mach. Tools Manuf.*, 2021, **165**, p 10-3729. <https://doi.org/10.1016/j.ijmactools.2021.103729>
2. S. Vock, B. Klöden, A. Kirchner, T. Weißgärber and B. Kieback, Powders for Powder Bed Fusion: A Review, *Prog. Addit. Manuf.*, 2019, **4**, p 383–397. <https://doi.org/10.1007/s40964-019-00078-6>
3. Y. Zhang, L. Wu, X. Guo, S. Kane, Y. Deng, Y.-G. Jung, J.-H. Lee and J. Zhang, Additive Manufacturing of Metallic Materials: A Review, *J. Mater. Eng. Perform.*, 2018, **27**, p 1–13. <https://doi.org/10.1007/s11665-017-2747-y>
4. I. La Fé-Perdomo, J.A. Ramos-Grez, G. Beruvides and R.A. Mujica, Selective Laser Melting: Lessons from Medical Devices Industry and Other Applications, *Rapid Prototyp. J.*, 2021, **27**(10), p 1801–1830. <https://doi.org/10.1108/RPJ-07-2020-0151>
5. J.A. Gonzalez, J. Mireles, S.W. Stafford, M.A. Perez, C.A. Terrazas and R.B. Wicker, Characterization of Inconel 625 Fabricated Using Powder-Bed-Based Additive Manufacturing Technologies, *J. Mater. Process. Technol.*, 2019, **264**, p 200–210. <https://doi.org/10.1016/j.jmptotec.2018.08.031>
6. S. Gruber, C. Grunert, M. Riede, E. Lopez, A. Marquardt, F. Brueckner and C. Leyens, Comparison of Dimensional Accuracy and Tolerances of Powder Bed Based and Nozzle Based Additive Manufacturing Processes, *J. Laser Appl.*, 2020, **32**, p 032016. <https://doi.org/10.2351/7.0000115>
7. D. Herzog, V. Seyd, E. Wycisk and C. Emmelmann, Additive Manufacturing of Metals, *Acta Mater.*, 2016, **117**, p 371–392. <https://doi.org/10.1016/j.actamat.2016.07.019>
8. P. Nandwana, A.M. Elliott, D. Siddel, A. Merriman, W.H. Peter and S.S. Babu, Powder Bed Binder jet 3D Printing of Inconel 718: Densification, Microstructural Evolution and Challenges, *Curr. Opin. Solid State Mater. Sci.*, 2017, **21**, p 207–218. <https://doi.org/10.1016/j.cossms.2016.12.002>
9. P.D. Enrique, E. Marzbanrad, Y. Mahmoodkhani, Z. Jiao, E. Toyserkani and N.Y. Zhou, Surface Modification of Binder-Jet Additive Manufactured Inconel 625 Via Electrospray Deposition, *Surf. Coat. Technol.*, 2019, **362**, p 141–149. <https://doi.org/10.1016/j.surfcoat.2019.01.108>
10. D.A. Lesyk, O.S. Lyman and V.V. Dzhemelinskiy, Surface characterization of the cobalt-based alloy stents fabricated by 3D laser metal fusion technology, *New Technol. Develop. Appl. III NT 2021. Lect. Notes Netw. Syst. I. Karabegović Ed.*, Springer International Publishing, 2021, p 357–364. https://doi.org/10.1007/978-3-030-75275-0_40
11. A. Hilaire, E. Andrieu and X. Wu, High-Temperature Mechanical Properties of Alloy 718 Produced by Laser Powder Bed Fusion with

Different Processing Parameters, *Addit. Manuf.*, 2019, **26**, p 147–16-0. <https://doi.org/10.1016/j.addma.2019.01.012>

12. P. Karimi, E. Sadeghi, J. Algardh and J. Andersson, EBM-Manufactured Single Tracks of Alloy 718: Influence of Energy Input and Focus Offset on Geometrical and Microstructural Characteristics, *Mater. Charact.*, 2019, **148**, p 88–99. <https://doi.org/10.1016/j.matchar.2018.11.033>
13. D.C. Kong, C.F. Dong, X.Q. Ni, L. Zhang, R.X. Li, X. He, C. Man and X.G. Li, Microstructure and Mechanical Properties of Nickel-Based Superalloy Fabricated by Laser Powder-Bed Fusion Using Recycled Powders, *Int. J. Miner. Metall. Mater.*, 2021, **28**, p 266–278. <https://doi.org/10.1007/s12613-020-2147-4>
14. D.A. Lesyk, S. Martinez, V.V. Dzhemelinskiy and A. Lamikiz, Additive manufacturing of the superalloy turbine blades by selective laser melting: Surface quality microstructure and porosity, *New Technol. Develop. Appl. III NT 2020 Lect. Notes Netw. Syst. I. Karabegović Ed.*, Springer International Publishing, 2020, p 267–27-5. https://doi.org/10.1007/978-3-030-46817-0_30
15. G.H. Cao, T.Y. Sun, C.H. Wang, X. Li, M. Liu, Z.X. Zhang, P.F. Hu, A.M. Russell, R. Schneider, D. Gerthsen, Z.J. Zhou, C.P. Li and G.F. Chen, Investigations of γ' , γ'' and δ Precipitates in Heat-Treated Inconel 718 Alloy Fabricated by Selective Laser Melting, *Mater. Charact.*, 2018, **136**, p 908–406. <https://doi.org/10.1016/j.MATCHAR.2018.01.006>
16. C. Panwisawas, Y. Tony Tang, J. Ghousoub and R.C. Reed, Additive manufacturability of nickel-based superalloys: Composition-process induced vaporization, *Superalloys*, (2020), p 1024–1032. https://doi.org/10.1007/978-3-030-51834-9_100
17. D.A. Lesyk, S. Martinez, B.N. Mordiyuk, V.V. Dzhemelinskiy and A. Lamikiz, Surface finishing of complexly shaped parts fabricated by selective laser melting, *Grabchenko's Int. Conf. Adv. Manuf. Proc. InterPartner-2019. Lect. Notes Mech. Eng.*, (2020), p 186–195. https://doi.org/10.1007/978-3-030-40724-7_19
18. D.A. Lesyk, S. Martinez, B.N. Mordiyuk, V.V. Dzhemelinskiy, A. Lamikiz and G.I. Prokopenko, Post-Processing of the Inconel 718 Alloy Parts Fabricated by Selective Laser Melting: Effects Of Mechanical Surface Treatments on Surface Topography, Porosity, Hardness and Residual Stress, *Surf. Coat. Technol.*, 2020, **381**, p 12-5136. <https://doi.org/10.1016/j.surfcoat.2019.125136>
19. I. Serrano-Munoz, T. Mishurova, T. Thiede, M. Sprengel, A. Kromm, N. Nadammal, G. Nolze, R. Saliwan-Neumann, A. Evans and G. Bruno, The Residual Stress in as-Built Laser Powder Bed Fusion IN718 Alloy as a Consequence of the Scanning Strategy Induced Microstructure, *Sci. Rep.*, 2020, **10**, p 14645. <https://doi.org/10.1038/s41598-020-71112-9>
20. A. Kreitzberg, V. Brailovski and S. Turenne, Effect of Heat Treatment and Hot Isostatic Pressing on the Microstructure and Mechanical Properties of Inconel 625 Alloy Processed by Laser Powder Bed Fusion, *Mater. Sci. Eng. A*, 2017, **689**(1), p 1–10. <https://doi.org/10.1016/j.msea.2017.02.038>
21. E.M. Fayed, M. Saadati, D. Shahriari, V. Brailovski, M. Jahazi and M. Medraj, Optimization of the Post-Process Heat Treatment of Inconel 718 Superalloy Fabricated by Laser Powder Bed Fusion Process, *Metals*, 2021, **11**, p 144. <https://doi.org/10.3390/met11010144>
22. G.E. Bean, T.D. McLouth, D.B. Witkin, S.D. Sitzman, P.M. Adams and R.J. Zaldivar, Build Orientation Effects on Texture and Mechanical Properties of Selective Laser Melting Inconel 718, *J. Mater. Eng. Perform.*, 2019, **28**, p 1942–1949. <https://doi.org/10.1007/s11665-019-03980-w>
23. R. Seede, A. Mostafa, V. Brailovski, M. Jahazi and M. Medraj, Microstructural and Microhardness Evolution from Homogenization and Hot Isostatic Pressing on Selective Laser Melted Inconel 718: Structure, Texture, and Phases, *Manuf. Mater. Process*, 2018, **2**, p 30–51. <https://doi.org/10.3390/jmmp2020030>
24. A. Vernouillet, A. Vande, A. Put, S.D. Pugliara and D. Monceau, Metal Dusting of Inconel 625 Obtained by Laser Beam Melting Effect of Manufacturing Process and Hot Isostatic Pressure Treatment, *Corros. Sci.*, 2020, **174**, p 108820. <https://doi.org/10.1016/j.corsci.2020.108820>
25. L.M. Roncery, I. Lopez-Galilea, B. Rutttert, D. Burger, P. Wollgramm, G. Eggeler and W. Theisen, On the Effect of Hot Isostatic Pressing on the Creep Life of a Single Crystal Superalloys, *Adv. Eng. Mater.*, 2016, **18**, p 1383–1387. <https://doi.org/10.1002/adem.201600071>
26. W. Tillmann, C. Schaak, J. Nellesen, M. Schaper, M.E. Aydinov and K.-P. Hoyer, Hot Isostatic Pressing of IN718 Components Manufac-

- tured by Selective Laser Melting, *Addit. Manuf.*, 2017, **13**, p 93–102. <https://doi.org/10.1016/j.addma.2016.11.006>
27. Y.L. Kuo, T. Nagahari and K. Kakehi, The Effect of Post-Processes on the Microstructure and Creep Properties of Alloy718 Built Up by Selective Laser Melting, *Mater.*, 2018, **11**, p 996–1009. <https://doi.org/10.3390/ma11060996>
 28. P. Liu, S. Sun, S. Xu, M. Cao, C. Hong and J. Hu, Effect of Solid Solution + Double Ageing on Microstructure and Properties in the Layer by Layer of the Z-Y Interface of Inconel 718 Alloys Fabricated by SLM, *Mater. Res.*, 2018, **21**, p e20180395. <https://doi.org/10.1590/1980-5373-MR-2018-0395>
 29. W.M. Tucho, P. Cuvillier, A. Sjolyst-Kverneland and V. Hansen, Microstructure and Hardness Studies of Inconel 718 Manufactured by Selective Laser Melting Before and After Solution Heat Treatment, *Mater. Sci. Eng. A*, 2017, **689**, p 220–232. <https://doi.org/10.1016/j.msea.2017.02.062>
 30. S. Raghavan, B. Zhang, P. Wang, C.-N. Sun, M.L.S. Nai, T. Li and J. Wei, Effect of Different Heat Treatments on the Microstructure and Mechanical Properties in Selective Laser Melted Inconel 718 Alloy, *Mater. Manuf. Process.*, 2017, **32**, p 1588–1595. <https://doi.org/10.1080/10426914.2016.1257805>
 31. J.A. Muñoz-Lerma, Y. Tian, X. Wang, R. Gauvin and M. Brochu, Microstructure Evolution of Inconel 738 Fabricated by Pulsed Laser Powder Bed Fusion, *Prog. Addit. Manuf.*, 2019, **4**, p 97–107. <https://doi.org/10.1007/s40964-018-0062-2>
 32. H.R. Javidrad and S. Salemi, Effect of the Volume Energy Density and Heat Treatment on the Defect, Microstructure, and Hardness of L-PBF Inconel 625, *Metall. Mater. Trans. A*, 2020, **51**, p 5880–5891. <https://doi.org/10.1007/s11661-020-05992-x>
 33. F. Brenne, A. Taube, M. Probstle, S. Neumeier, D. Schwarze, M. Schaper and T. Niendorf, Microstructural Design of Ni-Base Alloys for High-Temperature Applications: Impact of Heat Treatment on Microstructure and Mechanical Properties after Selective Laser Melting, *Prog. Addit. Manuf.*, 2016, **1**, p 141–151. <https://doi.org/10.1007/s40964-016-0013-8>
 34. E.M. Fayed, D. Shahriari, M. Saadati, V. Brailovski, M. Jahazi and M. Medraj, Influence of Homogenization and Solution Treatments Time on the Microstructure and Hardness of Inconel 718 Fabricated by Laser Powder Bed Fusion Process, *Mater.*, 2020, **13**, p 2574. <https://doi.org/10.3390/ma13112574>
 35. R. Barros, F.J.G. Silva, R.M. Gouveia, A. Saboori, G. Marchese, S. Biamino, A. Salmi and E. Atzeni, Laser Powder Bed Fusion of Inconel 718: Residual Stress Analysis Before and After Heat Treatment, *Metals*, 2019, **4**, p 97–107. <https://doi.org/10.3390/met9121290>
 36. Z. Baicheng, L. Xiaohua, B. Jiaming, G. Junfeng, W. Pan, S. Chen-nan, N. Muiling, Q. Guojun and W. Jun, Study of Selective Laser Melting (SLM) Inconel 718 Part Surface Improvement by Electrochemical Polishing, *Mater. Des.*, 2017, **116**, p 531–537. <https://doi.org/10.1016/j.matdes.2016.11.103>
 37. D.A. Lesyk, S. Martinez, V.V. Dzhemelinskyi, O. Stamann, B.N. Mordiyuk and A. Lamikiz, Surface polishing of laser powder bed fused superalloy components by magnetic post-treatment, *2020 IEEE 10th Int. Conf. Nanomater.: Appl. Propert. NAP-2020*, 2020, p 02SAMA17-1–02SAMA17-4. <https://doi.org/10.1109/NAP51477.2020.9309600>
 38. Y. Kaynak and E. Tascioglu, Post Processing Effects on the Surface Characteristics of Inconel 718 Alloy Fabricated by Selective Laser Melting Additive Manufacturing, *Prog. Addit. Manuf.*, 2020, **5**, p 221–234. <https://doi.org/10.1007/s40964-019-00099-1>
 39. A. Boschetto, L. Bottini, L. Macera and F. Veniali, Post-processing of Complex SLM Parts by Barrel Finishing, *Appl. Sci.*, 2020, **10**, p 13–82. <https://doi.org/10.3390/app10041382>
 40. J.D. Kim and I.S. Chao, Mechanical and Tribological Characteristics of Sintered Fe-Ni-Cr Alloy Subjected to High-Frequency Ultrasonic Peening, *Int. J. Surf. Sci. Eng.*, 2014, **8**, p 239–254. <https://doi.org/10.1504/IJSURFSE.2014.060488>
 41. D.A. Lesyk, V.V. Dzhemelinskyi, S. Martinez, B.N. Mordiyuk and A. Lamikiz, Surface Shot Peening Post-processing of Inconel 718 Alloy Parts Printed by Laser Powder Bed Fusion Additive Manufacturing, *J. Mater. Eng. Perform.*, 2021, **30**, p 6982–6995. <https://doi.org/10.1007/s11665-021-06103-6>
 42. D.A. Lesyk, S. Martinez, O.O. Pedash, V.V. Dzhemelinskyi and B.N. Mordiyuk, Combined thermo-mechanical techniques for post-processing of the SLM-printed Ni-Cr-Fe alloy parts, *Advances in Design, Simulation and Manufacturing III DSMIE 2020 Lecture Notes in Mechanical Engineering*. V. Ivanov et al., Ed., Springer International Publishing, 2020, p 295–304. https://doi.org/10.1007/978-3-030-50794-7_29
 43. O.V. Mythreyi, A. Raja, B.K. Nagesha and R. Jayaganthan, Corrosion Study of Selective Laser Melted IN718 Alloy Upon Post Heat Treatment and Shot Peening, *Metals*, 2020, **10**, p 1562. <https://doi.org/10.3390/met10121562>
 44. D.T. Ardi, L. Guowei, N. Maharjan, B. Mutiargo, S.H. Leng and R. Srinivasan, Effects of Post-processing Route on Fatigue Performance of Laser Powder Bed Fusion Inconel 718, *Addit. Manuf.*, 2020, **36**, p 101442. <https://doi.org/10.1016/j.addma.2020.101442>
 45. L. Hackel, J.R. Rankin, A. Rubenchik, W.E. King and M. Matthews, Laser Peening: A Tool for Additive Manufacturing Post-Processing, *Addit. Manuf.*, 2018, **24**, p 67–75. <https://doi.org/10.1016/j.addma.2018.09.013>
 46. K.L. Tan and S.H. Yeo, Surface Modification of Additive Manufactured Components by Ultrasonic Cavitation Abrasive Finishing, *Wear*, 2017, **378–379**, p 90–95. <https://doi.org/10.1016/j.wear.2017.02.030>
 47. Y. Vyshnepolskyi, D. Pavlenko, D. Tkach and Y. Dvirnyk, Parts diamond burnishing process regimes optimization made of INCONEL 718 alloy via selective laser sintering method, *2020 IEEE 10th Int. Conf. Nanomater.: Appl. Propert. NAP-2020*, 2020, p 02SAMA01-1–02SAMA01-5. <https://doi.org/10.1109/NAP51477.2020.9309661>
 48. S. Martinez, N. Ortega, D. Celentano, A.J.S. Egea, E. Ukar and A. Lamikiz, Analysis of the Part Distortions for Inconel 718 SLM: A Case Study on the NIST Test Artifact, *Mater.*, 2020, **13**, p 5087. <https://doi.org/10.3390/ma13225087>
 49. S. Sendino, M. Gardon, F. Lartategui, S. Martinez and A. Lamikiz, The Effect of the Laser Incidence Angle in the Surface of L-PBF Processed Parts, *Coatings*, 2020, **10**, p 1024. <https://doi.org/10.3390/coatings10111024>
 50. V.A. Popovich, E.V. Borisov, A.A. Popovich, V.S. Sufiarov, D.V. Masaylo and L. Alzina, Impact of Heat Treatment on Mechanical Behaviour of Inconel 718 Processed with Tailored Microstructure by Selective Laser Melting, *Mater. Des.*, 2017, **131**, p 12–22. <https://doi.org/10.1016/j.matdes.2017.05.065>
 51. J. Schröder, T. Mishurova, T. Fritsch, I. Serrano-Munoz, A. Evans, M. Sprengel, M. Klaus, C. Genzel, J. Schneider and G. Bruno, On the Influence of Heat Treatment on Microstructure and Mechanical Behavior of Laser Powder Bed Fused Inconel 718, *Mater. Sci. Eng. A*, 2021, **805**, p 140555. <https://doi.org/10.1016/j.msea.2020.140555>
 52. K. Moussaoui, W. Rubio, M. Mousseigne, T. Sultan and F. Rezai, Effects of Selective Laser Melting Additive Manufacturing Parameters of Inconel 718 on Porosity, Microstructure and Mechanical Properties, *Mater. Sci. Eng. A*, 2018, **735**, p 182–190. <https://doi.org/10.1016/j.msea.2018.08.037>
 53. R.G. Ding, Z.W. Huang, H.Y. Li, I. Mitchell, G. Baxter and P. Bowen, Electron Microscopy Study of Direct Laser Deposited IN718, *Mater. Charact.*, 2015, **106**, p 324–337. <https://doi.org/10.1016/j.matchar.2015.06.017>
 54. N.I. Khripta, O.P. Karasevska and B.N. Mordiyuk, Surface Layers of Zr-18% Nb Alloy Modified by Ultrasonic Impact Treatment: Microstructure, Hardness and Corrosion, *J. Mater. Eng. Perform.*, 2017, **26**, p 5446–5455. <https://doi.org/10.1007/s11665-017-2983-1>
 55. Y. Tian, D. McAllister, H. Colijn, M. Mills, D. Farson, M. Nordin and S. Babu, Rationalization of Microstructure heterogeneity in Inconel 718 Builds made by the Direct Laser Additive Manufacturing Process, *Met. Mat. Trans. A*, 2014, **45**, p 4470–4483. <https://doi.org/10.1007/s11661-014-2370-6>
 56. M. Renderos, A. Torregaray, M. Esther Gutierrez-Orrantia, A. Lamikiz, N. Saintier and F. Girot, Microstructure Characterization of Recycled IN718 Powder and Resulting Laser Clad Material, *Mater. Charact.*, 2017, **134**, p 103–113. <https://doi.org/10.1016/j.matchar.2017.09.029>
 57. Y. Zhao, K. Guan, Z. Yang, Z.P. Hu, Z. Qian, H. Wang and Z.Q. Ma, The Effect of Subsequent Heat Treatment on the Evolution Behavior of Second Phase Particles and Mechanical Properties of the Inconel 718 Superalloy Manufactured by Selective Laser Melting, *Mater. Sci. Eng. A*, 2020, **794**, p 139931. <https://doi.org/10.1016/j.msea.2020.139931>
 58. D. Cai, P. Nie, J. Shan, W. Liu, Y. Gao and M. Yao, Precipitation and Residual Stress Relaxation Kinetics in Shot-Peened Inconel 718, *J. Mater. Eng. Perform.*, 2006, **15**, p 614–617. <https://doi.org/10.1361/105994906X124613>
 59. A. Mostafa, I. Picazo Rubio, V. Brailovski, M. Jahazi and M. Medraj, Structure, Texture and Phases in 3D Printed IN718 Alloy Subjected to Homogenization and HIP Treatments, *Metals*, 2017, **7**, p 196. <https://doi.org/10.3390/met7060196>

60. R.J. Vikram, A. Singh and S. Suwas, Effect of Heat Treatment on the Modification of Microstructure of Selective Laser Melted (SLM) IN718 and its Consequences on Mechanical Behavior, *J. Mater. Res.*, 2020, **35**, p 1949–1962. <https://doi.org/10.1557/jmr.2020.129>
61. L.S.B. Ling, Z. Yin, Z. Hu, J.H. Liang, Z.-Y. Wang, J. Wang and B.D. Sun, Effects of the γ'' -Ni₃Nb Phase on Mechanical Properties of Inconel 718 Superalloys with Different Heat Treatments, *Mater.*, 2020, **13**, p 151. <https://doi.org/10.3390/ma13010151>
62. L. Zhou, A. Mehta, B. McWilliams, K. Cho and Y. Sohn, Microstructure, Precipitates and Mechanical Properties of Powder Bed Fused Inconel 718 Before and After Heat Treatment, *J. Mater. Sci. Technol.*, 2019, **35**, p 1153–1164. <https://doi.org/10.1016/j.jmst.2018.12.006>
63. N.C. Ferreri, S.C. Vogel and M. Knezevic, Determining Volume Fractions of γ , γ' , γ'' , δ , and MC-Carbide Phases in Inconel 718 as a Function of its Processing History Using an Advanced Neutron Diffraction Procedure, *Mater. Sci. Eng. A*, 2020, **781**, p 139228. <https://doi.org/10.1016/j.msea.2020.139228>
64. S. Yan, Y. Wang, Q. Wang, C. Zhang, D. Chen and G. Cui, Enhancing Mechanical Properties of the Spark Plasma Sintered Inconel 718 Alloy by Controlling the Nano-Scale Precipitations, *Mater.*, 2019, **12**, p 33–36. <https://doi.org/10.3390/ma12203336>
65. C. Kumara, A. Segerstark, F. Hanning, N. Dixit, S. Joshi, J. Moverare and P. Nylén, Microstructure Modelling of Laser Metal Powder Directed Energy Deposition of Alloy 718, *Addit. Manuf.*, 2019, **25**, p 357–364. <https://doi.org/10.1016/j.addma.2018.11.024>
66. F.C. Liu, F. Lyu, F.G. Liu, X. Lin and C. Huang, Laves Phase Control of Inconel 718 Superalloy Fabricated by Laser Direct Energy Deposition Via Aging and Solution Treatment, *J. Mater. Res. Technol.*, 2020, **9**, p 9753–9765. <https://doi.org/10.1016/j.jmrt.2020.06.061>
67. E.L. Stevens, J. Toman, A.C. To and M. Chmielus, Variation of Hardness, Microstructure, and Laves Phase Distribution in Direct Laser Deposited Alloy 718 Cuboids, *Mater. Des.*, 2017, **119**, p 188–198. <https://doi.org/10.1016/j.matdes.2017.01.031>
68. A. Bunsch, J. Kowalska and M. Witkowska, Influence of Die Forging Parameters on the Microstructure and Phase Composition of INCONEL 718 Alloy, *Arch. Met. Mater.*, 2012, **57**, p 929–935. <https://doi.org/10.2478/v10172-012-0102-8>
69. D.A. Lesyk, S. Martinez, O.O. Pedash, V.V. Dzhemelinskyi and A. Lamikiz, Porosity and Surface Defects Characterization of Hot Isostatically Pressed Inconel 718 Alloy Turbine Blades printed by 3D Laser Metal Fusion Technology, *MRS Adv.*, 2022. <https://doi.org/10.1557/s43580-021-00187-x>
70. Z. Tian, C. Zhang, D. Wang, W. Liu, X. Fang, D. Wellmann, Y. Zhao and Y. Tian, A Review on Laser Powder Bed Fusion of Inconel 625 Nickel-Based Alloy, *Appl. Sci.*, 2020, **10**, p 81. <https://doi.org/10.3390/app10010081>

Publisher's Note Springer Nature remains neutral with regard to jurisdictional claims in published maps and institutional affiliations.